

PAPER • OPEN ACCESS

## Deterministic direct growth of WS<sub>2</sub> on CVD graphene arrays

To cite this article: G Piccinini *et al* 2020 *2D Mater.* **7** 014002

View the [article online](#) for updates and enhancements.

### You may also like

- [Electronic structures and band alignment transition in double-wall MoS<sub>2</sub>/WS<sub>2</sub> nanotubes for optoelectronic applications](#)  
Dan Guo, Kaike Yang, Cai-Xin Zhang et al.
- [Correlating Microstructure and Activity for Polysulfide Reduction and Oxidation at WS<sub>2</sub> Electrocatalysts](#)  
Ifan E. L. Stephens, Caterina Ducati and Derek J. Fray
- [Ruthenium-decorated tungsten disulfide quantum dots for a CO<sub>2</sub> gas sensor](#)  
Keerti Rathi and Kaushik Pal

## OPEN ACCESS

## PAPER

Deterministic direct growth of WS<sub>2</sub> on CVD graphene arraysRECEIVED  
3 July 2019REVISED  
3 September 2019ACCEPTED FOR PUBLICATION  
1 October 2019PUBLISHED  
22 October 2019

Original content from  
this work may be used  
under the terms of the  
[Creative Commons  
Attribution 3.0 licence](#).

Any further distribution  
of this work must  
maintain attribution  
to the author(s) and the  
title of the work, journal  
citation and DOI.

G Piccinini<sup>1,2</sup>, S Forti<sup>1</sup>, L Martini<sup>1</sup>, S Pezzini<sup>1,3</sup>, V Miseikis<sup>1,3</sup> , U Starke<sup>4</sup> , F Fabbri<sup>1,3,5</sup> and C Coletti<sup>1,3</sup> <sup>1</sup> Center for Nanotechnology Innovation @NEST, Istituto Italiano di Tecnologia, Piazza San Silvestro 12, I-56127 Pisa<sup>2</sup> NEST, Scuola Normale Superiore, Piazza San Silvestro 12, I-56127 Pisa, Italy<sup>3</sup> Graphene Labs, Istituto Italiano di Tecnologia, Via Morego 30, I-16163 Genova, Italy<sup>4</sup> Max-Planck-Institut für Festkörperforschung, Heisenbergstraße 1, D-70569 Stuttgart, Germany<sup>5</sup> Present address: NEST, Istituto Nanoscienze—CNR, Scuola Normale Superiore, Piazza San Silvestro 12, I-56127 Pisa, ItalyE-mail: [camilla.coletti@iit.it](mailto:camilla.coletti@iit.it)**Keywords:** graphene, WS<sub>2</sub>, array, single crystal, CVD, synthesis, RamanSupplementary material for this article is available [online](#)**Abstract**

The combination of the exciting properties of graphene with those of monolayer tungsten disulfide (WS<sub>2</sub>) makes this heterostack of great interest for electronic, optoelectronic and spintronic applications. The scalable synthesis of graphene/WS<sub>2</sub> heterostructures on technologically attractive substrates like SiO<sub>2</sub> would greatly facilitate the implementation of novel two-dimensional (2D) devices. In this work, we report the direct growth of monolayer WS<sub>2</sub> via chemical vapor deposition (CVD) on single-crystal graphene arrays on SiO<sub>2</sub>. Remarkably, spectroscopic and microscopic characterization reveals that WS<sub>2</sub> grows only on top of the graphene crystals so that the vertical heterostack is selectively obtained in a bottom-up fashion. Spectroscopic characterization indicates that, after WS<sub>2</sub> synthesis, graphene undergoes compressive strain and hole doping. Tailored experiments show that such hole doping is caused by the modification of the SiO<sub>2</sub> stoichiometry at the graphene/SiO<sub>2</sub> interface during the WS<sub>2</sub> growth. Electrical transport measurements reveal that the heterostructure behaves like an electron-blocking layer at large positive gate voltage, which makes it a suitable candidate for the development of unipolar optoelectronic components.

**1. Introduction**

In the last few years, van der Waals heterostructures (vdWHs) based on graphene and transition metal dichalcogenides (TMDs) have emerged as promising candidates for a wide number of applications. TMDs have unique properties in the 2D limit, such as indirect-to-direct band gap transition [1], broad and strong absorption in the spectral range from ultraviolet to visible, large exciton binding energy [2], well-defined valley degrees of freedom and sizeable spin splitting of the valence band maximum (VBM) [3]. In particular, monolayer TMD/graphene stacks are vdWHs of interest since they combine the high carrier mobility of graphene [4] as well as the strong light-matter interactions of single layer TMD [5]. Indeed, such heterojunctions have already been exploited in functional architectures, such as photodetectors [6–14] and optospintronic devices [15, 16]. Furthermore, monolayer TMDs can be used on top of graphene not only as active materials to create vdWHs with enhanced electrooptical properties, but also as passive

encapsulants, to preserve graphene mobility [17]. However, to move towards realistic applications, it is fundamental to develop an entirely scalable approach for the fabrication of vdWHs. At present, chemical vapor deposition (CVD) is the most suitable technique for the scalable synthesis of highly-crystalline 2D heterostructures [18, 19]. The direct synthesis of WS<sub>2</sub> on graphene reduces the number of transfer steps, simplifying the fabrication process and is an ideal approach to obtain an atomically sharp interface [20].

To date, few works have demonstrated the direct synthesis of WS<sub>2</sub> on polycrystalline CVD graphene to obtain vertical [21] or lateral [10, 13] heterostructures, the latter for the fabrication of photodetectors. Rossi *et al* have shown the patterned synthesis of WS<sub>2</sub> on epitaxial graphene on silicon carbide (SiC) and the photodetection performance of such heterostructure [14]. However, no work has yet reported the direct synthesis of WS<sub>2</sub> on scalable high-mobility single-crystal CVD graphene on SiO<sub>2</sub>, an appealing platform for the development of optoelectronic devices. Also, the effect of WS<sub>2</sub> growth on the properties of the underlying

graphene crystal has been to date overlooked. Indeed, a thorough understanding of the influence of the direct CVD growth of WS<sub>2</sub> on the electronic and structural properties of single-crystal graphene is instrumental for identifying optimal paths to obtain performing and atomically sharp vdWHs.

In this work, we demonstrate the direct CVD growth of a single WS<sub>2</sub> layer on graphene single crystal arrays, deterministically grown via CVD on copper (Cu) foil and transferred on a technologically relevant substrate (i.e. SiO<sub>2</sub>) [18, 22]. The scalable synthetic approach demonstrated here is suitable for the implementation of microelectronic and optoelectronic devices. We thoroughly characterize the heterostack via Raman spectroscopy, photoluminescence (PL) spectroscopy, scanning electron microscopy (SEM), x-ray photoemission spectroscopy (XPS) and electrical transport measurements. Raman spectroscopy indicates that, upon WS<sub>2</sub> growth, graphene exhibits compressive strain and p-type doping, the latter caused by decomposition of the SiO<sub>2</sub> substrate as confirmed by XPS measurements. Furthermore, we present electrical transport measurements performed on the synthesized heterostack. The resistance as a function of gate voltage shows a significant electron-hole asymmetry, due to the presence of sulfur vacancies in WS<sub>2</sub> which form a trap level for graphene electrons. This hole-transporting/electron-blocking property could be conveniently employed for the development of unipolar optoelectronic components.

## 2. Methods

Graphene single crystal arrays [23–25] with a lateral size of about 200 μm were deterministically synthesized via CVD on electropolished copper (Cu) foils (Alfa Aesar, 99.8%) following the procedure described by Miseikis *et al* [18]. The Cu foils were selectively patterned using chromium (Cr) disks, which act as nucleation seeds for graphene crystals. Graphene was then synthesized at a temperature of 1060 °C inside a cold-wall CVD system (Aixtron BM) under methane, hydrogen and argon flow. The crystals were subsequently transferred on SiO<sub>2</sub>/Si substrates (285 nm thick SiO<sub>2</sub> layer on p-doped Si, Sil'tronix) using a semi-dry procedure [18, 22]. Specifically, a poly(methyl methacrylate) (PMMA AR-P 679.02 Allresist GmbH) film was used to support the graphene single crystals while detaching them from Cu using electrochemical delamination. The PMMA-coated graphene array was subsequently aligned with the target Si/SiO<sub>2</sub> substrate using a micromechanical stage and finally deposited on it. More details about the graphene growth and the transfer technique can be found in the supplementary information ([stacks.iop.org/TDM/7/014002/mmedia](https://stacks.iop.org/TDM/7/014002/mmedia)).

WS<sub>2</sub> was grown directly on graphene on SiO<sub>2</sub> via CVD from solid precursors, i.e. tungsten trioxide WO<sub>3</sub> and sulfur S. The process was performed in a 2.5" horizontal hot-wall furnace. As sketched in figure S2, the

furnace comprises a central hot-zone, where a crucible with the WO<sub>3</sub> powder was placed 20 mm away from the growth substrate, and an inlet zone heated by a resistive belt, in which the S powder was positioned, in order to separately control its temperature. S was evaporated and then carried by an argon flux to the centre of the furnace where it reacted with WO<sub>3</sub> directly on the sample surface at a temperature of 900 °C and at a pressure of  $\sim 5 \times 10^{-2}$  mbar, see supplementary information for additional details. The growth time necessary for a full coverage of the graphene crystals was 20 min. Partial growths, instrumental to assess the size and orientation of the WS<sub>2</sub> crystals, were carried out decreasing the growth time down to 5 min. Such partial growths yielded a WS<sub>2</sub> coverage of graphene of about 80% (see figure 1(b)).

The exfoliated h-BN flakes used in this work were purchased from HQ Graphene.

Thermal annealing experiments were performed in an ultra-high vacuum (UHV) chamber (base pressure of  $2 \times 10^{-10}$  mbar). Temperature ramp up/down rates of 1 °C min<sup>-1</sup> were used and the target temperatures were maintained for 10 h.

Raman spectroscopy was used to assess crystal quality, doping and strain of graphene and was performed together with PL to characterize quality and thickness of WS<sub>2</sub>. Both Raman and PL measurements were carried out with a Renishaw InVia spectrometer equipped with a 532 nm laser with a spot size of  $\sim 1$  μm. The power used was 1 mW.

SEM was performed to study the morphology of each sample. A Zeiss Merlin microscope and electrons with an accelerating voltage of 5 kV were used.

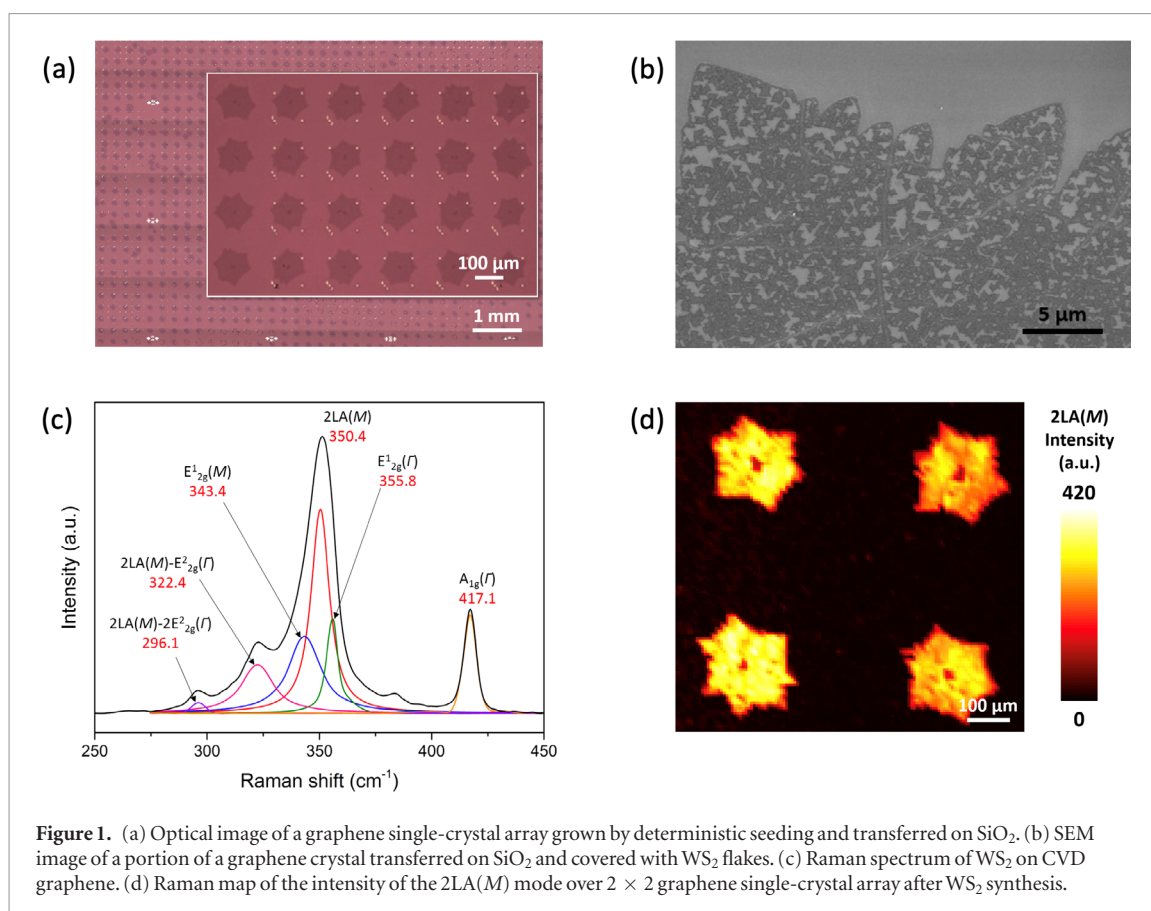
X-ray photoelectron spectroscopy (XPS) measurements were performed at room temperature with a Mg Kα anode coupled to a Phoibos150 electron analyzer from SPECS GmbH. The photoemission angle used was 60° with respect to the surface normal in order to increase the surface sensitivity of the measurements. The binding energies of the peaks reported in the text were referenced to the energy of graphene sp<sup>2</sup> carbon set at 284.5 eV.

To investigate the transport characteristics of graphene after WS<sub>2</sub> growth, multi-terminal field-effect transistor (FET) devices were fabricated on WS<sub>2</sub>/graphene/SiO<sub>2</sub>. Electric-field effect measurements were performed at room temperature using a Keithley 2450 sourcemeter with a micro-probe station in air. By applying a constant current of 1 μA between the external electrodes, we measured the voltage drop along the device as function of the applied back-gate voltage ( $V_{bg}$ ).

## 3. Results and discussion

### 3.1. WS<sub>2</sub>/graphene scalable heterostructures

Figure 1(a) shows the typical graphene single-crystal array grown by deterministic seeding and transferred on SiO<sub>2</sub> [18] adopted to perform CVD growth of WS<sub>2</sub>.



This synthetic approach of graphene has significant prospects for scalability and is flexible, i.e. single crystals of different size and spacing can be obtained. While reducing transfer related problems (i.e. tears and breaks are reduced when transferring smaller tiles rather than continuous wafers), this approach also allows to have high-mobility graphene exactly where needed [18]. Indeed, the positioning of the crystal can be flexibly designed accordingly to the mask of any final optoelectronic device.

In initial experiments, partial growth of WS<sub>2</sub> was performed to assess dimension and orientation of the crystals of the synthesized TMD on graphene. A SEM image of a portion of a graphene crystal covered with WS<sub>2</sub> flakes is displayed in figure 1(b). The WS<sub>2</sub> triangular crystals have dimensions of a few hundred nanometers and most of them are merged with adjacent ones. A higher density of WS<sub>2</sub> flakes is clearly visible along the graphene wrinkles, indicating that the morphology of the underlying graphene layer, in particular the presence of defects, strongly affects WS<sub>2</sub> nucleation. WS<sub>2</sub> crystals present only two different orientations related to each other by a rotation of 60°. This suggests the existence of an epitaxial relation between WS<sub>2</sub> and graphene, which was already reported for monolayer WS<sub>2</sub> directly grown on 2D materials [19, 21, 26, 27].

A typical Raman spectrum of the synthesized WS<sub>2</sub>, probed with a 532 nm laser, is displayed in figure 1(c). The Raman feature around 350 cm<sup>-1</sup> is the

convolution of the four peaks 2LA(M) – E<sub>2g</sub><sup>2</sup>(Γ), E<sub>2g</sub><sup>1</sup>(M), 2LA(M), and E<sub>2g</sub><sup>1</sup>(Γ), while the peak A<sub>1g</sub>(Γ) at 417.1 cm<sup>-1</sup> is a first-order mode corresponding to out-of-plane oscillations of atoms. When using a specific excitation wavelength, the second-order phonon mode 2LA(M) is more prominent than the in-plane phonon mode E<sub>2g</sub><sup>1</sup>(Γ) and the 2LA(M)/A<sub>1g</sub>(Γ) intensity ratio is used as indicative parameter of the thickness of WS<sub>2</sub> [28]. A 2LA(M)/A<sub>1g</sub>(Γ) intensity ratio above 2, as in this case, is typical of monolayer WS<sub>2</sub> crystals [28]. Photoluminescence spectra reported in supplementary figure S3 further confirm that WS<sub>2</sub> is single-layer.

Remarkably, panel (b) suggests that WS<sub>2</sub> crystals only grow on the graphene flakes and not on the SiO<sub>2</sub> substrate, probably owing to the desorption of oxygen from SiO<sub>2</sub> which hinders the sulfurization of the WO<sub>3</sub> precursor (for further information see section 3.4 and figure S8 in supplementary information). In order to confirm what is observed by SEM, we performed scanning Raman spectroscopy experiments. Figure 1(d) shows a Raman map of the intensity of the 2LA(M) mode over 2 × 2 graphene single-crystal array after WS<sub>2</sub> synthesis. Indeed, WS<sub>2</sub> growth seems to be strongly favored on the graphene substrate: no WS<sub>2</sub> Raman signatures are detected on SiO<sub>2</sub> (for additional Raman analysis see supplementary figure S3). The selective growth of WS<sub>2</sub> crystals on the graphene flakes represents a clear advantage for the fabrica-

tion of devices as the entire vertical heterostructure is deterministically obtained in arrays without the need of any top-down post-processing.

### 3.2. Effect of the direct synthesis of WS<sub>2</sub> on graphene: doping and strain

In order to investigate the full applicative potential of the heterostack and to further develop the materials synthesis, it is crucial to characterize the properties of the CVD graphene crystals after WS<sub>2</sub> growth, something that to date has not yet been exhaustively addressed. We adopt Raman spectroscopy as a powerful tool yielding insights on the structural and electronic properties of graphene. In the case of single-layer graphene, any shift of the two prominent G and 2D Raman peaks is attributable to strain [29, 30] and/or doping [31–34] in the material. In figure 2(a) we show the Raman spectra of graphene before and after WS<sub>2</sub> synthesis. A considerable stiffening of both characteristic modes, G (26.5 cm<sup>-1</sup> blue-shift) and 2D (35 cm<sup>-1</sup> blue-shift), is consistently observed after WS<sub>2</sub> growth. Notably, no increase in the intensity of the negligible D-peak is observed, indicating that the growth process does not induce significant defects in the crystal structure of the underlying graphene. The significant blue-shift of the 2D peak observed after WS<sub>2</sub> growth typically indicates that the majority carriers in graphene are holes [33]. A correlation plot of the G and 2D peak positions ( $\omega_G$  and  $\omega_{2D}$  respectively)—instrumental to disentangle the strain and doping contribution [35, 36]—is shown in panel (b). The two solid lines are the directions along which the strain-induced (purple line) and the hole doping-induced (orange line) shifts are expected [35]. The intersection of the two lines ( $\omega_G^0, \omega_{2D}^0$ ) = (1583, 2678) cm<sup>-1</sup> represents the case of neutral and unstrained graphene [33]. The data plotted in panel (b) are extracted from representative 15 × 15 μm<sup>2</sup> analyzed areas. Remarkably, the graphene crystals transferred by semi-dry process (black data points) are in close proximity to the unstrained and undoped reference, differently from wet-transferred CVD graphene where residual doping >10<sup>12</sup> cm<sup>-2</sup>—caused by the transfer process—is typically found [37–40]. After WS<sub>2</sub> growth, the graphene crystals present compressive strain and hole doping estimated to be about 0.6% and 10<sup>13</sup> cm<sup>-2</sup>, respectively (red data points). The increase in doping is also confirmed by the strong reduction of the intensity of the 2D peak with respect to the intensity of the G peak (figure 2(c)) [31, 41, 42]. Furthermore, the significant enlargement of the 2D full-width-at-half-maximum (FWHM) value upon WS<sub>2</sub> growth (figure 2(d)), from a remarkably low 24 cm<sup>-1</sup> to about 37 cm<sup>-1</sup>, suggests an increase of the strain fluctuation in the graphene crystal [43], a possible limiting factor for the carrier mobility in this vdWH.

### 3.3. Effect of thermal annealing on CVD single-crystal graphene properties

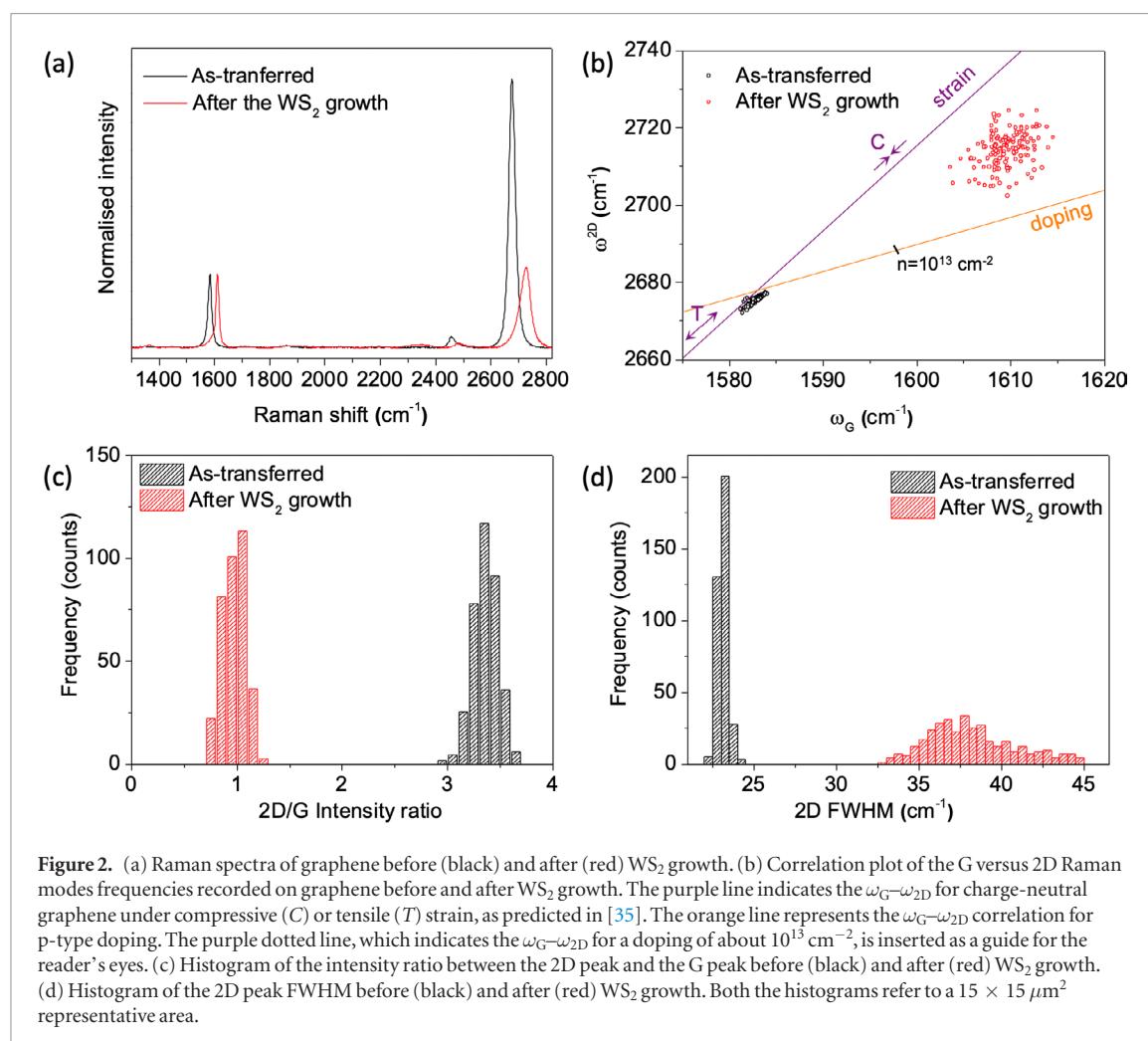
In order to assess the influence of the high-temperature annealing (carried out during the growth process) on graphene strain and doping, annealing processes were performed in a controlled atmosphere. One sample was annealed at 900 °C (i.e. WS<sub>2</sub> growth temperature) under Ar flux, in order to replicate the conditions experienced by the sample during the CVD growth of WS<sub>2</sub> (same time and pressure, but without the presence of solid precursors). Two other samples were annealed in UHV, one at 300 °C and the other at 500 °C.

We find that when annealing the sample at 300 °C, the Raman fingerprint of graphene is only slightly affected while more substantial changes are observed for the 500 °C and 900 °C annealing stages (see figure 3(a) and supplementary figure S5). Indeed, the  $\omega_{2D}-\omega_G$  correlation plot indicates a little increase of hole doping for the 300 °C annealing and the emergence of a stronger doping entirely comparable to that observed after WS<sub>2</sub> synthesis (i.e. 10<sup>13</sup> cm<sup>-2</sup>) for higher annealing temperatures. Remarkably, the central values of the dataset distributions relating to as-transferred and annealed graphene, have almost the same projection onto the strain axis. This indicates that thermal treatments carried out in these specific experimental conditions contribute mostly to the doping, which reaches its maximum value already at 500 °C. This finding is qualitatively in agreement to what was reported for polycrystalline CVD graphene heated under He atmosphere by Costa *et al* [44], although in the correlation plot we retrieve smaller data spreads for the pristine and low-temperature annealed samples, as a consequence of the higher quality and homogeneity of single-crystal graphene.

These data also suggest that the compressive strain observed in graphene after WS<sub>2</sub> growth is largely due to the interaction with the overlying material. The model we propose is that, in virtue of its negative thermal expansion coefficient [45–47], graphene lattice parameters get reduced during the heating. When WS<sub>2</sub> nucleates on such a compressed lattice, it may find a more stable configuration for forming a coincidence lattice with graphene, locking graphene in the strained configuration. In a previous work we found that WS<sub>2</sub> on epitaxial graphene, which is characterized by a compressed lattice, form a (7 × 7) on a (9 × 9) superperiodicity with graphene [48]. Admitting that as a sort of natural coincidence lattice, graphene should shrink by about 0.45%, a value in line with what is extracted from the Raman analysis above.

### 3.4. The origin of doping in annealed CVD graphene on SiO<sub>2</sub>

Having clarified that graphene hole doping upon WS<sub>2</sub> growth is a result of the thermal annealing of

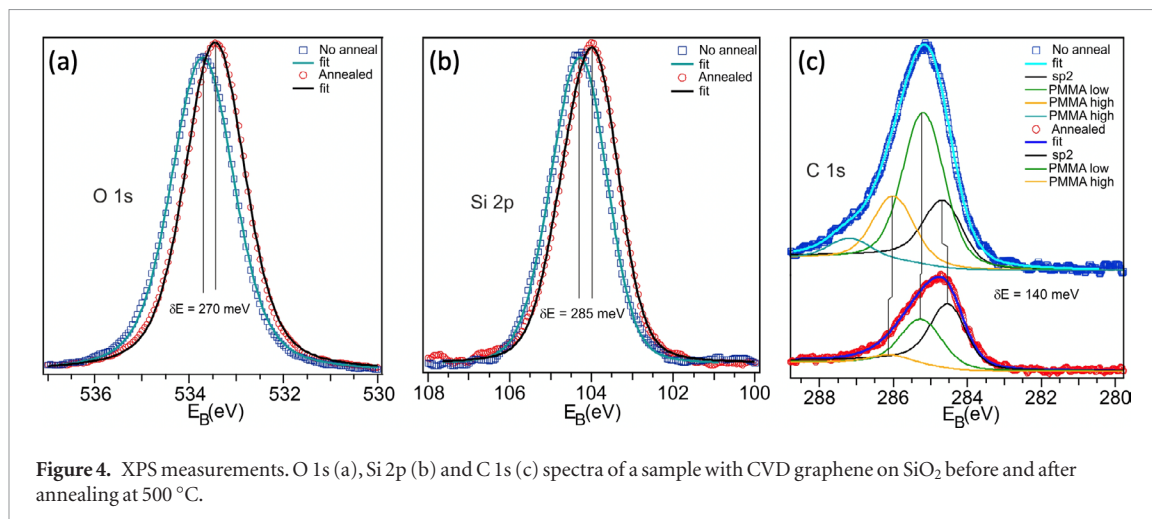
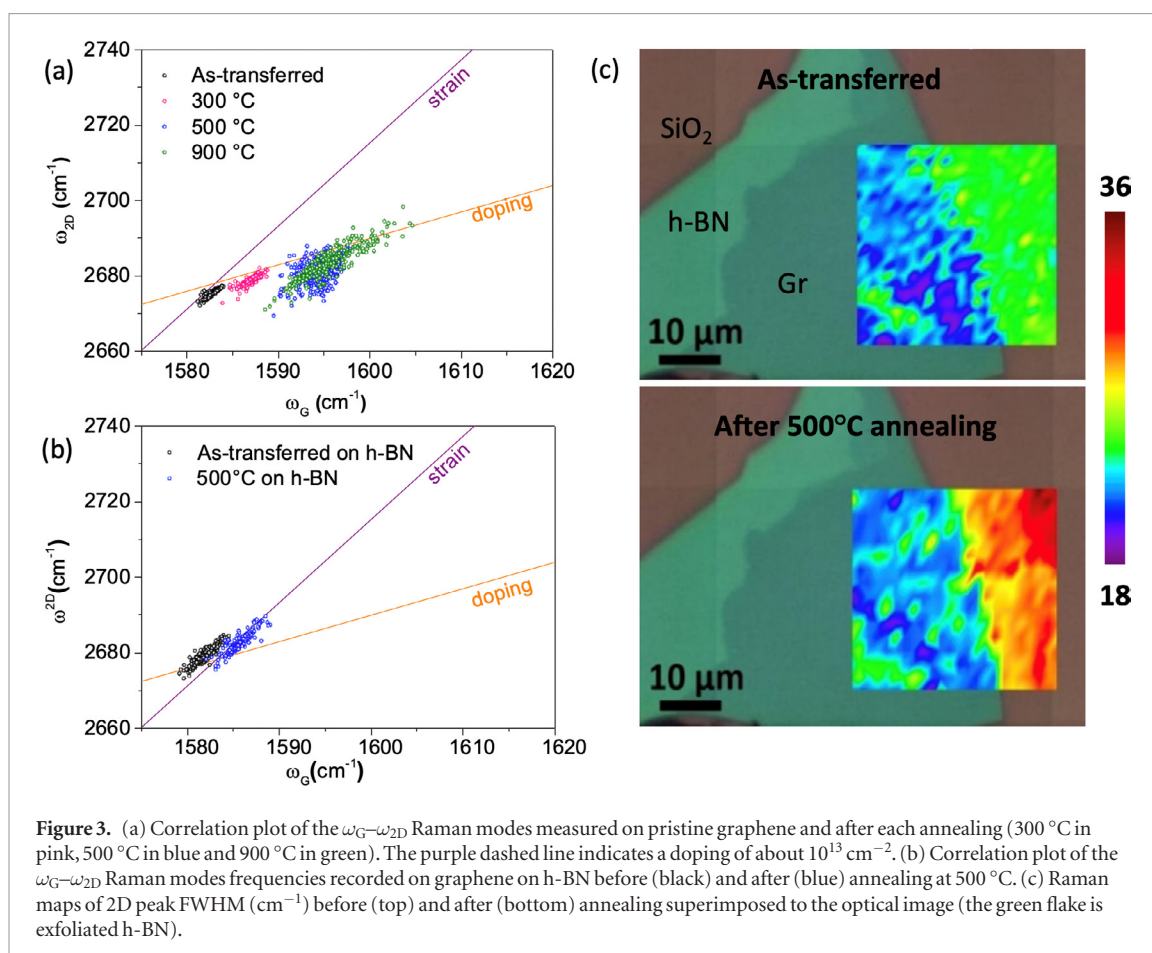


the sample, we now focus on identifying the physico-chemical origin of such doping. To date, a number of works have attributed hole doping of annealed exfoliated graphene on SiO<sub>2</sub> to ambient H<sub>2</sub>O and O<sub>2</sub> molecules adsorbed owing to thermal-induced structural deformation or defects [44, 49–52]. Other works have instead suggested that the hole doping is mostly induced by the SiO<sub>2</sub> substrate, that upon annealing experiences an enhanced coupling with graphene [44, 53, 54]. In order to understand whether the doping is substrate- or atmosphere-induced, we carried out a comparative experiment. A large CVD graphene crystal was transferred partly on an exfoliated hexagonal boron nitride (h-BN) flake (~20 nm thick) and partly directly on top of SiO<sub>2</sub> and then annealed at 500 °C in UHV. h-BN, indeed, is well-known as an ideal and effective encapsulant for graphene [55], capable of screening doping from the substrate and atmosphere when used as a bottom- or top-encapsulant, respectively [56].

Raman characterization, performed after extracting the sample from the vacuum chamber, showed that the annealing did not induce either significant doping or strain (see correlation plot in panel (b)) in the graphene portion placed on top of h-BN. In contrast, the portion on SiO<sub>2</sub> shows the same distribution as the blue one in panel (a). Furthermore, Raman maps in

figure 3(c) report a significant broadening of the 2D peak for annealed graphene on SiO<sub>2</sub>, while no broadening is observed upon the annealing of graphene on h-BN. This result rules out molecular adsorption due to air exposure as a possible cause for the measured doping. If the doping was due to the environment, we would expect a similar hole doping level for both the graphene/h-BN and the graphene/SiO<sub>2</sub> region. Furthermore, differently from previous works [44, 49, 50–52] in our system WS<sub>2</sub> acts as a top-encapsulant, hindering atmospheric-induced doping of graphene. Therefore, the doping originates from graphene/SiO<sub>2</sub> interface states activated by thermal annealing. XPS measurements performed on a sample with CVD graphene on SiO<sub>2</sub> before and after annealing at 500 °C in UHV corroborate this thesis.

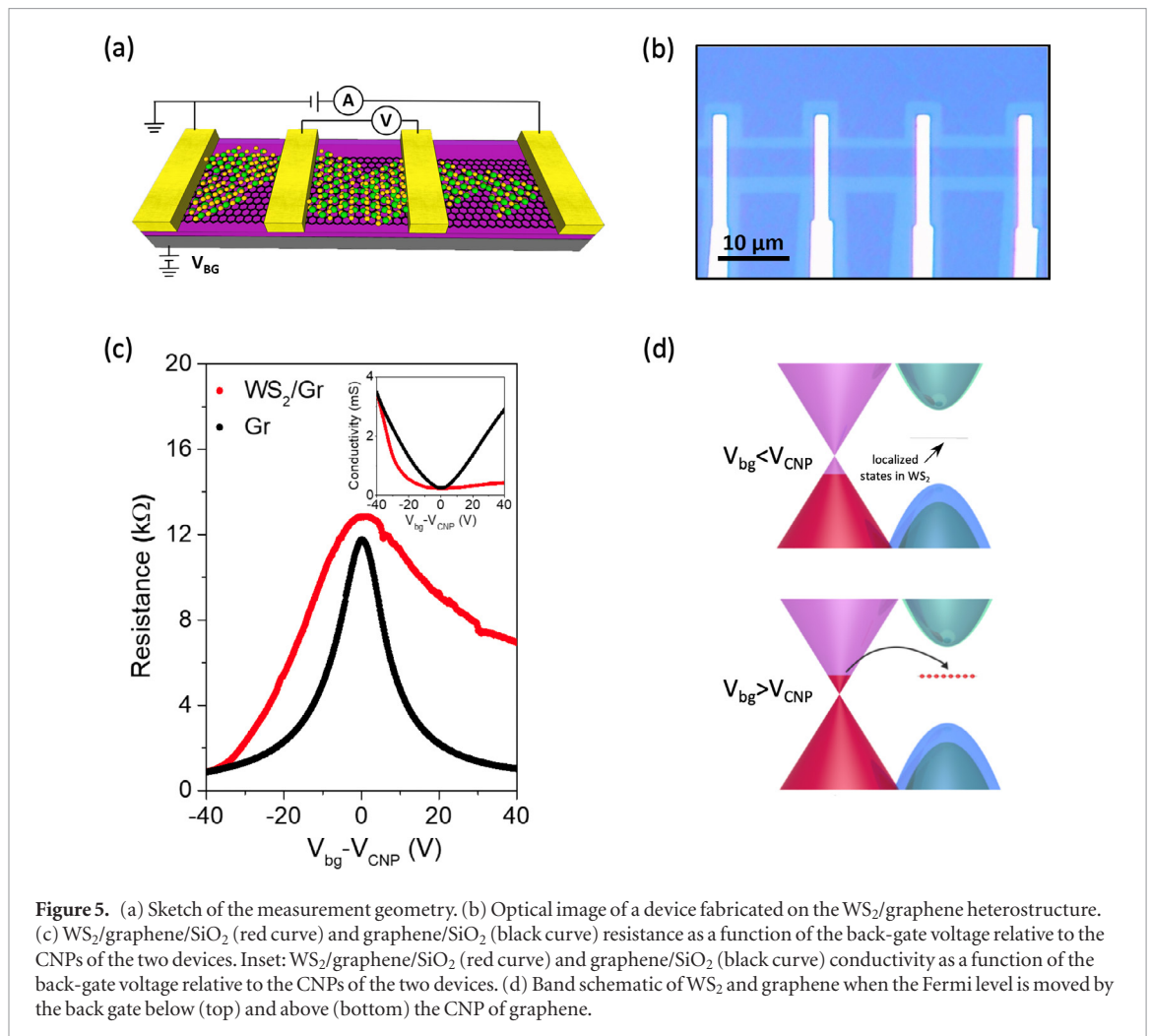
We display the results of those measurements in figure 4. Panels (a) and (b) show a clear decrease of the binding energy for the O 1s and Si 2p peaks upon annealing, which indicates an oxygen loss from the top layers of the substrate, yielding a graphene/SiO<sub>(2-δ)</sub> interface. Such an under stoichiometric interface generates a polarization field the net effect of which is the p-type doping of graphene. The apparent increase of the peak intensity after the annealing is attributed to carbon contaminants, which are desorbed from the surface. This is well visible when looking at the C 1s



peak, reported in figure 4(c). The C 1s peak shifts as a whole by about 450 meV, again towards lower binding energies. However, we identify at least four components in the peak before annealing and three after annealing. It is well known that after standard cleaning procedures [40, 57–59] residues of the PMMA layer used during transfer are still present on the graphene surface. We therefore assign the three components of the C 1s peak considerably reduced upon thermal treatment (i.e. due to evaporation of the polymer from the surface) to polymeric residues. The component at lowest binding energy which is not affected by the

annealing is assigned to sp $^2$  bound carbon, i.e. graphene. The sp $^2$  carbon component shows a net shift by about 140 meV towards lower binding energy. Since for small deviations the shift of the binding energy and the graphene doping are linearly related [59], we can conclude that the XPS data is qualitatively in agreement with the Raman data, ultimately confirming a displacement towards higher p-type doping of the annealed graphene layer (more details can be found in supplementary figure S6).

In virtue of what is shown in figure 3, we propose inserting a protective layer (possibly another 2D



material) between graphene and the substrate to avoid p-type doping of graphene during CVD growth or other high-temperature process.

### 3.5. Electrical transport measurements

The electrical properties of the synthesized WS<sub>2</sub>/graphene vdWH were assessed via four-contact electrical measurements (figure 5(a)) in ambient conditions. A typical WS<sub>2</sub>/graphene multi-terminal field-effect transistor (FET) device is shown in figure 5(b) (details on the device fabrication can be found in supplementary figure S7). In figure 5(c) we show the resistance of the vdWH (red curve) and that of a reference pristine CVD single-crystal graphene (black curve) as a function of the voltage ( $V_{bg}$ ) applied to the back gate (p-doped Si wafer with 285 nm of thermal oxide). The two devices have equal geometry and have undergone the same fabrication steps, making their resistance curves directly comparable. To make the comparison between the two transfer characteristics easier, along the  $x$ -axis we put the  $V_{bg}$  relative to the charge neutrality points (CNPs) of the two devices. The CNP in the after-WS<sub>2</sub>-growth case, indeed, was measured at higher positive gate voltages ( $\sim 20.5$  V for the least doped measured sample) with respect to the graphene-only case ( $\sim 12.4$  V),

confirming again that the CVD process for WS<sub>2</sub> synthesis dopes graphene with holes. In particular, the hole density at  $V_{bg} = 0$  for this particular device, estimated by the CNP shift, is  $n_h \sim 1.5 \times 10^{12} \text{ cm}^{-2}$ .

While the black curve shows the typical symmetric peak of graphene, a marked electron-hole asymmetry is observed for the vdWH, with the red trace almost pinned to the resistance value at the CNP. This is assigned to the presence of sulfur vacancies in WS<sub>2</sub>, identified via XPS analysis (see supplementary figure S8). These vacancies in the WS<sub>2</sub> layer trap the electrons induced by gating in the contiguous graphene layer (figure 5(d)). The saturation of the resistance curve for the vdWH can be easily attributed to having a small density of electrons in the graphene sheet and contributing to the conductance, despite the large gate voltage applied, with the ‘missing’ carriers occupying WS<sub>2</sub> defect states. A similar (although less marked) effect of hole–electron asymmetry in WS<sub>2</sub>/graphene vdWH was reported by Avsar *et al* [15] using mechanically exfoliated WS<sub>2</sub>, which are free from grain boundaries and with a low edges/area ratio. Since flake’s edges are the points where sulfur vacancies are mostly concentrated in TMDs [60], the enhancement of the electron-hole asymmetry in our experiment can be easily explained. This asymmetry in the conduction



of holes and electrons can be conveniently exploited in a number of applications ranging from energy conversion to optical detection. For example, in solar cells, this heterostack used as an anode contact could help to optimize the collection of the photogenerated holes, blocking the electrons at the same time [61, 62]. Furthermore, considering the extremely fast charge transfer already demonstrated between the two materials [63, 64] this deterministically grown entirely scalable vdWH could be exploited to develop unipolar devices for optoelectronics and optospintronics.

#### 4. Conclusions


In this work, we demonstrate the direct synthesis of monolayer WS<sub>2</sub> on single-crystal CVD graphene arrays. We observe a selective growth of WS<sub>2</sub> crystals on graphene, a clear advantage for the fabrication of devices as the vertical heterostructure is deterministically obtained in arrays without the need of any top-down post-processing. The presented heterostructure has the advantages of being fully scalable and compatible with a silicon technology platform. We also investigate the structural and electrical properties of graphene after WS<sub>2</sub> growth. The graphene substrate turns out to be affected by hole doping and compressive strain. While the strain is attributed to the interaction with the WS<sub>2</sub> overlayer, thermal treatment experiments allow us to assign the doping of graphene to SiO<sub>2</sub> interface states activated by the high temperatures during the TMD synthesis. We demonstrate that a protective layer such as h-BN placed between graphene and the SiO<sub>2</sub> substrate before growth is instrumental to avoid the doping. Finally, we show that the heterostructure behaves like an electron-blocking layer, which might be suitable for the development of unipolar components in optoelectronics.

#### Acknowledgments

The authors would like to thank Mauro Gemmi, Simona Pace and Antonio Rossi from CNI@NEST for support in TEM imaging.

The research leading to these results has received funding from the European Union's Horizon 2020 research and innovation program under grant agreement No. 785219—GrapheneCore2.

#### ORCID iDs

V Miseikis  <https://orcid.org/0000-0001-6263-4250>  
 U Starke  <https://orcid.org/0000-0003-1153-1862>  
 C Coletti  <https://orcid.org/0000-0002-8134-7633>

#### References

- [1] Zhang Y, Chang T, Zhou B, Cui Y, Yan H and Liu Z 2013 Direct observation of the transition from indirect to

direct bandgap in atomically thin epitaxial MoSe<sub>2</sub> *Nat. Nanotechnol.* **9** 111–5

- [2] Hanbicki A T, Currie M, Kioseoglou G, Friedman A L and Jonker B T 2015 Measurement of high exciton binding energy in the monolayer transition-metal dichalcogenides WS<sub>2</sub> and WSe<sub>2</sub> *Solid State Commun.* **203** 16–20
- [3] Xu X, Yao W, Xiao D and Heinz T F 2014 Spin and pseudospins in layered transition metal dichalcogenides *Nat. Phys.* **10** 343–50
- [4] Bolotin K I, Sikes K J, Jiang Z, Klima M, Fudenberg G, Hone J, Kim P and Stormer H L 2008 Ultrahigh electron mobility in suspended graphene *Solid State Commun.* **146** 351–5
- [5] Britnell L et al 2013 Strong light-matter interactions thin films *Science* **340** 1311–4
- [6] Zhang W et al 2014 Ultrahigh-Gain Photodetectors Based on Atomically Thin Graphene-MoS<sub>2</sub> Heterostructures *Sci. Rep.* **4** 3826
- [7] Lan C, Li C, Wang S, He T, Zhou Z, Wei D, Liua G, Yang H and Yong L 2017 Highly responsive and broadband photodetectors based on WS<sub>2</sub>-graphene van der Waals epitaxial heterostructures *J. Mater. Chem. C* **5** 1494–500
- [8] Han P, Marie L S, Wang Q X and Quirk N 2018 Highly sensitive MoS<sub>2</sub> photodetectors with graphene contacts *Nanotechnology* **29** 20LT01
- [9] Wei X, Yan F-G, Shen C, Lv Q-S and Wang K-Y 2017 Photodetectors based on junctions of two-dimensional transition metal dichalcogenides *Chin. Phys. B* **26** 038504
- [10] Deng W, Chen Y, You C, Liu B, Yang Y and Shen G 2018 High detectivity from a lateral graphene—MoS<sub>2</sub> Schottky photodetector grown by chemical vapor deposition *Adv. Electronic Mater.* **4** 1800069
- [11] Sun B, Shi T, Liu Z, Wu Y, Zhou J and Liao G 2018 Large-area flexible photodetector based on atomically thin MoS<sub>2</sub>/graphene film *Mater. Des.* **154** 1–7
- [12] Huang H, Sheng Y, Zhou Y, Zhang Q, Hou L, Chen T, Chang R and Warner J H 2018 2D-layer-dependent behavior in lateral Au/WS<sub>2</sub>/graphene photodiode devices with optical modulation of Schottky barriers *ACS Appl. Nano Mater.* **1** 6874–81
- [13] Chen T, Sheng Y, Zhou Y, Chang R, Wang X, Huang H, Zhang Q, Hou L and Warner J H 2019 High photoresponsivity in ultrathin 2D lateral graphene:WS<sub>2</sub>:graphene photodetectors using direct CVD growth *ACS Appl. Mater. Interfaces* **11** 6421–30
- [14] Rossi A, Spirito D, Bianco F, Forti S, Fabbri F, Büch H, Tredicucci A, Krahn R and Coletti C 2018 Patterned tungsten disulfide/graphene heterostructures for efficient multifunctional optoelectronic devices *Nanoscale* **10** 4332–8
- [15] Avsar A et al 2014 Spin-orbit proximity effect in graphene *Nat. Commun.* **5** 4875
- [16] Luo Y K, Xu J, Zhu T, Wu G, McCormick E J, Zhan W, Neupane M R and Kawakami R K 2017 Opto-valleytronic spin injection in monolayer MoS<sub>2</sub>/few-layer graphene hybrid spin valves *Nano Lett.* **17** 3877–83
- [17] Kretinin A V et al 2014 Electronic properties of graphene encapsulated with different two-dimensional atomic crystals *Nano Lett.* **14** 3270–6
- [18] Miseikis V, Bianco F, David J, Gemmi M, Pellegrini V, Romagnoli M and Coletti C 2017 Deterministic patterned growth of high-mobility large-crystal graphene: a path towards wafer scale integration *2D Mater.* **4** 021004
- [19] Rossi A, Büch H, Di Rienzo C, Miseikis V and Convertino D 2016 Scalable synthesis of WS<sub>2</sub> on graphene and h-BN: an all-2D platform for light-matter transduction *2D Mater.* **3** 031013
- [20] Büch H, Rossi A, Forti S, Convertino D, Tozzini V and Coletti C 2018 Superlubricity of epitaxial monolayer WS<sub>2</sub> on graphene *Nano Res.* **11** 5946–5956
- [21] Bianco G V, Losurdo M, Giangregorio M M, Sacchetti A, Prete P, Lovergine N, Capezzuto P and Bruno G 2015 Direct epitaxial CVD synthesis of tungsten disulfide on epitaxial and CVD graphene *RSC Adv.* **5** 98700–8
- [22] Miseikis V et al 2015 Rapid CVD growth of millimetre-sized single crystal graphene using a cold-wall reactor *2D Mater.* **2** 014006

- [23] Wu W, Jauregui L A, Su Z, Liu Z, Bao J, Chen P and Yu Q 2011 Growth of single crystal graphene arrays by locally controlling nucleation on polycrystalline Cu using chemical vapor deposition *Adv. Mater.* **23** 4898–903
- [24] Yu Q et al 2011 Control and characterization of individual grains and grain boundaries in graphene grown by chemical vapour deposition *Nat. Mater.* **10** 443–9
- [25] Song X, Gao T, Nie Y, Zhuang J, Sun J, Shi J, Lin Y, Ding F, Zhang Y and Liu Z 2016 Seed-assisted growth of single-crystalline patterned graphene domains on hexagonal boron nitride by chemical vapor deposition *Nano Lett.* **16** 6109–16
- [26] Kobayashi Y, Sasaki S, Mori S, Hibino H, Liu Z and Watanabe K 2015 Growth and optical properties of high-quality monolayer WS<sub>2</sub> on graphite *ACS Nano* **9** 4056–63
- [27] Okada M, Sawazaki T, Watanabe K, Taniguchi T, Hibino H, Shinohara H and Kitaura R 2014 Direct chemical vapor deposition growth of WS<sub>2</sub> atomic layers on hexagonal boron nitride *ACS Nano* **8** 8273–7
- [28] Berkdemir A et al 2013 Identification of individual and few layers of WS<sub>2</sub> using Raman Spectroscopy *Sci. Rep.* **3** 1755
- [29] Mohiuddin T M G et al 2009 Uniaxial strain in graphene by Raman spectroscopy: G peak splitting, Grüneisen parameters, and sample orientation *Phys. Rev. B* **79** 205433
- [30] Huang M, Yan H, Heinz T F and Hone J 2010 Probing strain-induced electronic structure change in graphene by Raman spectroscopy *Nano Lett.* **10** 4074–9
- [31] Kalbac M, Reina-Cecco A, Farhat H, Kong J, Kavan L, Dresselhaus M S and Heyrovsky J 2010 The influence of strong electron and hole doping on the raman intensity of chemical vapor-deposition graphene *ACS Nano* **4** 6055–63
- [32] Casiraghi C, Pisana S, Novoselov K S, Geim A K and Ferrari A C 2007 Raman fingerprint of charged impurities in graphene *Appl. Phys. Lett.* **91** 233108
- [33] Das A et al 2008 Monitoring dopants by Raman scattering in an electrochemically top-gated graphene transistor *Nat. Nanotechnol.* **3** 210–5
- [34] Froehlicher G and Berciaud S 2015 Raman spectroscopy of electrochemically gated graphene transistors: geometrical capacitance, electron-phonon, electron-electron, and electron-defect scattering *Phys. Rev. B* **91** 205413
- [35] Lee J E, Ahn G, Shim J, Lee Y S and Ryu S 2012 Optical separation of mechanical strain from charge doping in graphene *Nat. Commun.* **3** 1024
- [36] Mueller N S, Heeg S, Pe M, Kusch P, Wasserroth S and Clark N 2017 Evaluating arbitrary strain configurations and doping in graphene with Raman spectroscopy *2D Mater.* **5** 015016
- [37] Suk J W, Lee W H, Lee J, Chou H, Piner R D, Hao Y, Akinwande D and Ruo R S 2013 Enhancement of the electrical properties of graphene grown by chemical vapor deposition via controlling the effects of polymer residue *Nano Lett.* **13** 1462–7
- [38] Lupina G et al 2015 Residual metallic contamination of transferred chemical vapor deposited graphene *ACS Nano* **9** 4776–85
- [39] Kim S, Shin S, Kim T, Du H, Song M, Lee C, Kim K, Cho S, Seo D H and Seo S 2016 Robust graphene wet transfer process through low molecular weight polymethylmethacrylate *Carbon* **98** 352–7
- [40] Park H, Lim C, Lee C and Kang J 2018 Optimized poly (methyl methacrylate)—mediated graphene-transfer process for fabrication of high-quality graphene layer *Nanotechnology* **29** 415303
- [41] Basko D M, Piscanec S and Ferrari A C 2007 Electron-electron interactions and doping dependence of the two-phonon Raman intensity in graphene *Phys. Rev. B* **80** 165413
- [42] Casiraghi C 2009 Doping dependence of the Raman peaks intensity of graphene near the Dirac point *Phys. Rev. B* **80** 233407
- [43] Neumann C et al 2015 Raman spectroscopy as probe of nanometre-scale strain variations in graphene *Nat. Commun.* **6** 8429
- [44] Costa S D, Weis J E, Frank O, Fridrichová M and Kalbac M 2016 Monitoring the doping of graphene on SiO<sub>2</sub>/Si substrates during the thermal annealing process *RSC Adv.* **6** 72859–64
- [45] Nelson J B and Ryley D P 1945 The thermal expansion of graphite from 15 °C to 800 °C: part I. Experimental *Proc. Phys. Soc.* **57** 477
- [46] Bonini N, Lazzeri M, Marzari N and Mauri F 2007 Phonon Anharmonicities in Graphite and Graphene *Phys. Rev. Lett.* **99** 176802
- [47] Yoon D, Son Y-W and Cheong H 2011 Negative thermal expansion coefficient of graphene measured by Raman spectroscopy *Nano Lett.* **11** 3227–3231
- [48] Forti S et al 2017 Electronic properties of single-layer tungsten disulfide on epitaxial graphene on silicon carbide *Nanoscale* **9** 16412–9
- [49] Ryu S, Liu L, Berciaud S, Yu Y J, Liu H, Kim P, Flynn G W and Brus L E 2010 Atmospheric oxygen binding and hole doping in deformed graphene on a SiO<sub>2</sub> substrate *Nano Lett.* **10** 4944–51
- [50] Ni Z H, Wang H M, Luo Z Q, Wang Y Y, Yu T, Wu Y H and Shen Z X 2010 The effect of vacuum annealing on graphene *J. Raman Spectrosc.* **41** 479–83
- [51] Levesque P L, Sabri S S, Aguirre C M, Guillemette J, Siaz M, Desjardins P, Szkopek T and Martel R 2011 Probing charge transfer at surfaces using graphene transistors *Nano Lett.* **11** 132–7
- [52] You A, Be M A Y and In I 2017 Oxygen sensors made by monolayer graphene under room temperature *Appl. Phys. Lett.* **99** 243502
- [53] Sabio J, Seoáñez C, Fratini S, Neto A H C and Sols F 2008 Electrostatic interactions between graphene layers and their environment *Phys. Rev. B* **77** 195409
- [54] Cheng Z, Zhou Q, Wang C, Li Q, Wang C and Fang Y 2011 Toward intrinsic graphene surfaces: a systematic study on thermal annealing and wet-chemical treatment of SiO<sub>2</sub>-supported graphene devices *Nano Lett.* **11** 767–71
- [55] Dean C R et al 2010 Boron nitride substrates for high-quality graphene electronics *Nat. Nanotechnol.* **5** 722–6
- [56] Engels S, Terrés B, Klein F, Reichardt S, Goldsche M, Kuhlen S, Watanabe K, Taniguchi T and Stampfer C 2014 Impact of thermal annealing on graphene devices encapsulated in hexagonal boron nitride *Phys. Status Solidi b* **251** 2545–50
- [57] Li R, Li Z, Pambou E, Gutfreund P, Waigh T A, Webster J R P and Lu J R 2018 Determination of PMMA residues on a chemical-vapor-deposited monolayer of graphene by neutron Reflection and atomic force microscopy *Langmuir* **34** 1827–33
- [58] Islam A E, Zakharov D N, Carpena-Nuñez J, Hsiao M, Drummy L F, Stach E A and Maruyama B 2017 Atomic level cleaning of poly-methyl-methacrylate residues from the graphene surface using radiolized water at high temperatures *Appl. Phys. Lett.* **111** 103101
- [59] Schröder U A, Petrović M, Gerber T, Martínez-Galera A J, Grånäs E, Arman M A, Herbig C, Schnadt J, Kralj M and Knudsen J 2016 Core level shifts of intercalated graphene *2D Mater.* **4** 015013
- [60] Fabbri F et al 2016 Novel near-infrared emission from crystal defects in MoS<sub>2</sub> multilayer flakes *Nat. Commun.* **7** 13044
- [61] Chen L, Xu Z, Hong Z and Yang Y 2010 Interface investigation and engineering—achieving high performance polymer photovoltaic devices *J. Mater. Chem.* **20** 2575–98
- [62] Naja L et al 2018 MoS<sub>2</sub> quantum dot graphene hybrids for advanced interface engineering of a CH<sub>3</sub>NH<sub>3</sub>PbI<sub>3</sub> perovskite solar cell with an efficiency of over 20% *ACS Nano* **12** 10736–54
- [63] Aeschlimann S, Rossi A, Krause R, Arnoldi B, Aeschlimann M, Forti S, Fabbri F and Coletti C Direct evidence for efficient ultrafast charge separation in epitaxial WS<sub>2</sub>/graphene heterostructure (arXiv:1904.01379)
- [64] Yuan L, Chung T, Kuc A, Wan Y, Xu Y, Chen Y P, Heine T and Huang L 2018 Photocarrier generation from interlayer charge-transfer transitions in WS<sub>2</sub>-graphene heterostructures *Sci. Adv.* **4** e1700324